Applied Ocean Research 55 (2016) 76–88

Contents lists available at ScienceDirect

Applied Ocean Research

journal homepage: www.elsevier.com/locate/apor

Investigation of a longfin inshore squid's swimming characteristics and an underwater locomotion during acceleration

Mahdi Tabatabaei Malazi [a], Ali Bahadir Olcay [b,*]

[a] Yildiz Technical University, Faculty of Mechanical Engineering, Besiktas, Istanbul 34349, Turkey
[b] Yeditepe University, Mechanical Engineering Department, Atasehir, Istanbul 34755, Turkey

ARTICLE INFO

Article history:
Received 11 June 2015
Received in revised form
11 December 2015
Accepted 12 December 2015
Available online 29 December 2015

Keywords:
Longfin inshore squid
Computed tomography (CT)
CFD
Propulsive efficiency
Drag
Unsteady fluid flow

ABSTRACT

In the present study, locomotion of a real longfin inshore squid (*Doryteuthis pealeii*) was numerically investigated. Geometry of a real squid was obtained using computed tomography (CT) images. In addition to a two-dimensional axisymmetric squid model, a modified squid model with no cavities around her head and an ellipse shaped model were generated with a fineness ratio (the ratio of body length to maximum body diameter) of 7.56. These numerical models were exposed to an acceleration with two different velocity programs. Added mass and basset forces on bodies were calculated during acceleration of the squid models starting from rest. Pressure and viscous drag forces were also calculated due to pressure variation along the squid models and friction on the surface of the models. The effect of a nozzle diameter on jet velocities and propulsive efficiency at all bodies were evaluated when time dependent velocity profiles (from 0 to 10 m/s in 0.5 and 1 s time durations) were set for the inlet of computational domain. The modified squid model required least thrust force during acceleration phase of time dependent velocity profile compared to the other models while the 0.02 m nozzle diameter provided largest propulsive efficiency for all models.

1. Introduction

Many technological developments were inspired by nature creating new ideas and techniques. The design of an underwater vehicle is one of the applications of nature motivated by aquatic animals. It was realized that mimicking an aquatic animals' body shape could help us improve a drag coefficient of an underwater vehicle such as a submarine. When aquatic creatures are considered, a squid exhibits a unique swimming method because of her ad hoc locomotion system. Briefly, a squid can eject the water already drawn into her mantle cavity to accelerate. A squid can actually achieve 30–40 km/h speed in less than a second by her amazing jet propulsion system. Furthermore, a squid having a well streamlined body shape has a reduced drag coefficient while jet propulsion and fins are used for fast and slow swimming, respectively.

In literature, Bartol et al. [1] investigated three different boxfish shapes. They studied pressure, velocity distribution and force balance on boxfishes by using digital partial image velocimetry (DPIV). They also stated that boxfishes can move very stable at high velocities in water; therefore, the design of car bodies was influenced from boxfishes. Stelle et al. [2] studied drag forces measurement of Steller sea lions in different swimming velocities and deceleration during glide swimming conditions in a seawater tank. They recorded some videos during swimming of sea lions in the tank and their results covered measurement of drag forces for 66 glides from six juvenile sea lions. They documented the mean drag coefficient to be 0.0056 at Reynolds number of 5,500,000 where the total wetted surface area was taken as a reference area of drag in their calculations. When underwater swimming is considered, understanding added mass plays an important role because initially fluid in front of a body must be moved out of the way for the body to accelerate. The force required to move this mass is named added mass force. Lin and Liao [3] calculated added mass coefficient by fast the multiple boundary element method (FMBEM) in 3-D underwater bodies. They tested this method on different bodies such as a sphere and SUBOFF submarine. They stated that their results using FMBEM method provided efficient findings with already tabulated coefficients. Ghassemi and Yari [4] also investigated the added mass coefficient of ellipsoid, sphere and hydrofoil by using the numerical boundary element method (BEM) in water.

Abbreviations: RANS, Reynolds-averaged Navier–Stokes; FMBEM, fast multiple boundary element method; BEM, boundary element method; DPIV, digital partial image velocimetry; VOF, volume of fluid; UDF, user define function; SST, shear stress transport; AUV, autonomous underwater vehicle; CT, computed tomography.

* Corresponding author. Tel.: +90 2165780461; fax: +90 2165780400.
E-mail address: bahadir.olcay@yeditepe.edu.tr (A.B. Olcay).

0141-1187/$ – see front matter © 2015 Elsevier Ltd. All rights reserved.
http://dx.doi.org/10.1016/j.apor.2015.12.002

Nomenclature

A_{jet}	cross-sectional area of the jet
A	squid wetted surface area
$A_{surface}$	surface area of the squid
C_D	drag coefficient
t	total simulation/acceleration time
t'	the instantaneous time
$u(t)$	velocity of the body
D	mantle cavity diameter
D_{nozzle}	nozzle diameter
F_D	drag force
F_T	thrust force
$F_{D\_viscous}$	viscous drag force
$F_{D\_pressure}$	pressure drag force
$U_{vehicle}$	underwater vehicle velocity
L	squid body length
L/D	fineness ratio
Re	Reynolds number
U_{jet}	jet velocity
U	free stream velocity
G_k	turbulence kinetic energy generation
G_ω	generation of ω
Γ_k	effective diffusivity of k
Γ_ω	diffusivity of ω
Y_k	dissipation of k due to turbulence
Y_ω	dissipation of ω due to turbulence
D_ω	represents the cross-diffusion term
S_k	user-defined source term
S_ω	user-defined source term

Greek symbols

η	propulsive efficiency
ρ	density of fluid
ρ_c	carrier fluid's density
μ	dynamic viscosity of fluid
μ_c	carrier fluid's dynamic viscosity

They showed that the BEM method has good accuracy for calculating added mass coefficient than other numerical models. On the other hand, Korotkin [5] emphasized the importance of added mass for bodies starting motion from rest. They documented an added mass coefficient diagram of an ellipsoid for variety of major to minor axis ratio values. It was noted that added mass force could be calculated once the added mass coefficient was obtained from the diagram for bodies resembling an ellipsoid shape. Jagadeesh and Murali [6] worked on the influence of free surface effects on hydrodynamic coefficients of an axisymmetric underwater body. They used Reynolds-averaged Navier–Stokes (RANS) model and their focus remained on the capabilities of the turbulence models. It was documented that prediction of free surface wave effects on hydrodynamic coefficients for model was superior with k–ε realizable model with (volume of fluid) VOF method. The effects of fin and jet propulsion during a squid's swimming were experimentally studied by Anderson and Grosenbaugh [7]. They showed that a squid can change the shape of her fin and jet propulsion nozzle to control dynamic balance at different speeds especially in acceleration phase. Their study also indicated that squids use their fins for low swimming speeds and jet propulsion for high swimming speeds. Stewart et al. [8] studied the effect of squids' fin at forward locomotion. They applied 2-D DPIV technique to observe vortexes and understand the effect of lift force at varying degrees of a fin during swimming. They also investigated various swimming positions at different fin positions. Moslemi and Krueger [9] were motivated by squids and built a mechanical Robosquid. This underwater vehicle used pulsed-jet to accelerate. Although Robosquid had some differences compared to a real squid, they were able to investigate propulsive efficiency of an underwater vehicle experimentally by using DPIV. Their study covered Reynolds number range between 1300 and 2700 based on average vehicle velocity and diameter of the vehicle. Two different jet velocity profiles (triangular and trapezoidal) were used in jet slug length-to-diameter ratio in the range between 2 and 6. They concluded that higher duty cycle value and lower jet slug length-to-diameter ratio caused increased efficiency of pulsed jet propulsion to the equivalent steady jet propulsion. Moslemi and Krueger [10] in another study examined the Reynolds number effect on a self-propelled and pulsed-jet of the Robosquid. They documented that the average propulsive efficiency decreased by 26% when the Reynolds number was decreased from 2000 to 50 and the ratio of pulsed-jet to steady jet efficiency increased up to 0.15. Shereena et al. [11] investigated drag reduction in axisymmetric underwater vehicles with air jet injection in the boundary layer numerically. They utilized a SST k–ω turbulence model and mixture model for the multiphase flow. Different air jet velocity to body velocity ratios, various angles of air jet and body's angles of attack were tested. They reported that the effect of tapered to blunt aft shape had an important influence on drag reduction performance. Recently, Mansoorzadeh and Javanmard [12] examined the drag and lift coefficients of an autonomous underwater vehicle (AUV) using experimental and numerical methods. Their experimental and computational models investigated different Reynolds numbers from 1.9 to 3.17 million. Their results show that speed of the AUV highly affects AUV's drag and lift coefficients. Bettle et al. [13] simulated submarine maneuvers by using numerical methods. They studied emergency rising and horizontal zig-zag maneuvers by an implicit predictor–corrector method solving for two different iterative schemes (under-relaxed fixed-point and Newton iteration methods) and the results of these methods were compared. The Newton iteration method was chosen for this study. More recently, Nematollahi et al. [14] considered an axisymmetric underwater vehicle at various depths and velocities. They studied numerically hydrodynamic characteristics of an underwater vehicle by using ANSYS-CFX software and the total drag coefficient was calculated at different speeds ranging from 0.4 to 1.4 m/s at various depths. Hydrodynamic interaction between underwater bodies in relative motion were lately studied by Randeni et al. [15]. They provided validation of their CFD model based on the results of towing tank experiments. Hydrodynamic coefficients of an AUV was estimated by the proposed simplified method with superposition of steady-state interaction force coefficient to the single body hydrodynamic coefficient and they noted that the variation stayed below 14%.

The objective of this study is to investigate the swimming performance of a real squid, a modified squid and ellipsoid body shape models numerically by using two different velocity programs. The amount of thrust force required to follow a desired velocity program were identified for the studied models. On the other hand, as squids have a flexible nozzle tissue, it was also decided to evaluate the effect of nozzle diameter on propulsion efficiency.

2. Materials and methods

2.1. Computed tomography (CT) scans of squids

When aquatic life is considered, the squid, a member of cephalopods, exhibits a quite unique swimming performance under water. A squid typically move by ejecting pressurized water through her nozzle. Briefly, a squid has a flexible mantle tissue where she can draw water and keep it inside this tissue as shown in Fig. 1. Prior to movement, a squid contracts her circular

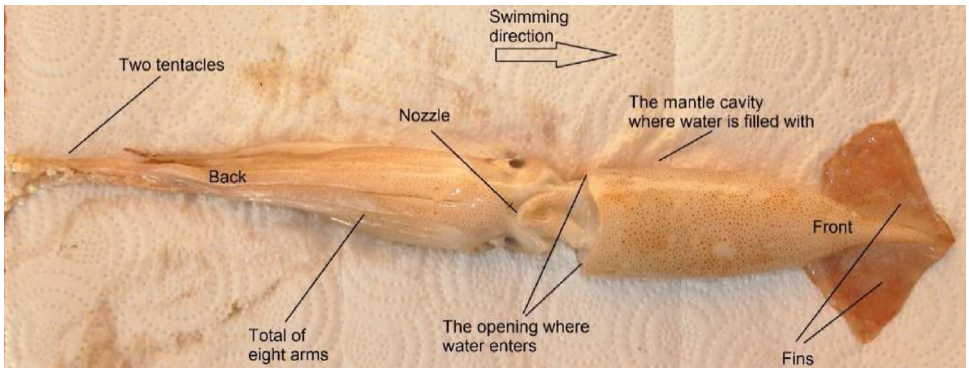

Fig. 1. Anatomy of a squid.

Fig. 2. Computed tomography (CT) machine and placement of squids prior to scanning.

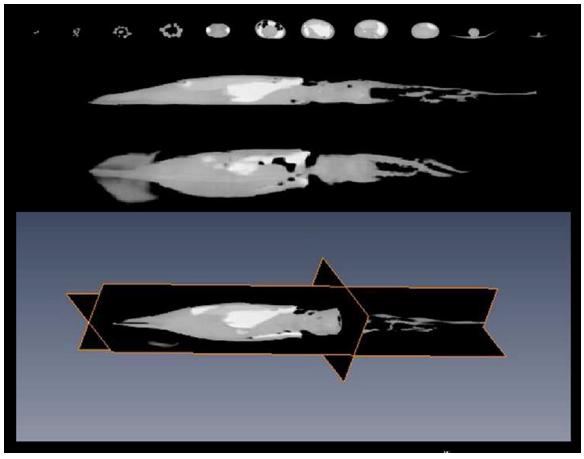

Fig. 3. Computed tomography scans provided set of dicom images. Above: Layers were formed from images for every 30° angle scan between 0° and 360°. Below: a side view, a top view and a composite view.

muscles located around the mantle tissue. This contraction increases pressure of water inside the mantle cavity up to 25 kPa (gage). She then squirts this pressurized water to the opposite direction of where she needs to move so that she can accelerate into her desired direction. In the present work, a longfin inshore squid specifically member of the loliginidae family (*Doryteuthis pealeii*) was studied to obtain geometry of the squid by taking computed tomography (CT) images using Philips Brilliance CT 64-channel machine. Preliminary computed tomography scan results showed that flatness on dead squids became an issue since live squids did not have any flatness during swimming. To prevent flatness, silicone gels were injected inside the mantle cavity of the squids and once the silicone gels were dried out, squids were positioned for CT scan as shown in Fig. 2. Dicom format image set was obtained from CT scanning and the outer surface of the squid was constructed from a set of 360 images presenting layer by layer x-ray scans as shown in Fig. 3. Meshlab Software (v1.3.1 Visual Computing Lab) was used to export the surface formed by small triangles in .stl format. Once the constructed surface was obtained, double nodes and small voids defects were located and repaired by using a surface detection algorithm. When the legs and tentacles of a hanging downward squid were considered, irregular voids were present as illustrated in Fig. 4. Thus, these voids in each image were filled and the image contrast was raised; as a result, soft tissue could be clearly distinguished from its surroundings. Lastly, the number of triangles defining the surface was reduced with the help of quadratic edge collapse decimation algorithm and a smoothing algorithm was finally applied on the images layer by layer to achieve a smooth surface as shown in Fig. 5.

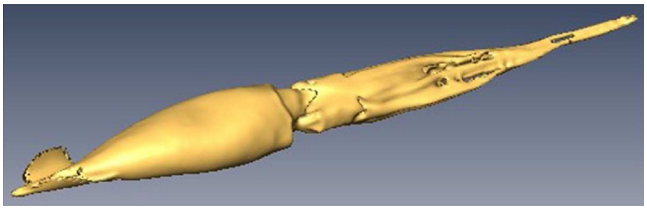

Fig. 4. Image layers were used to construct squid's surface.

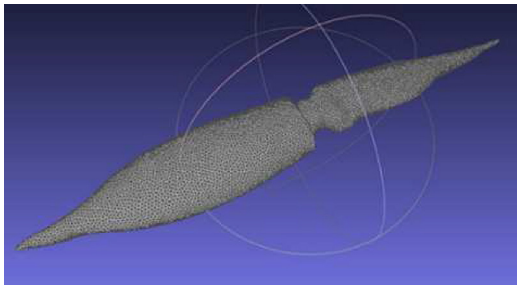

Fig. 5. Surface model after segmentation, defect cleaning and smoothing.

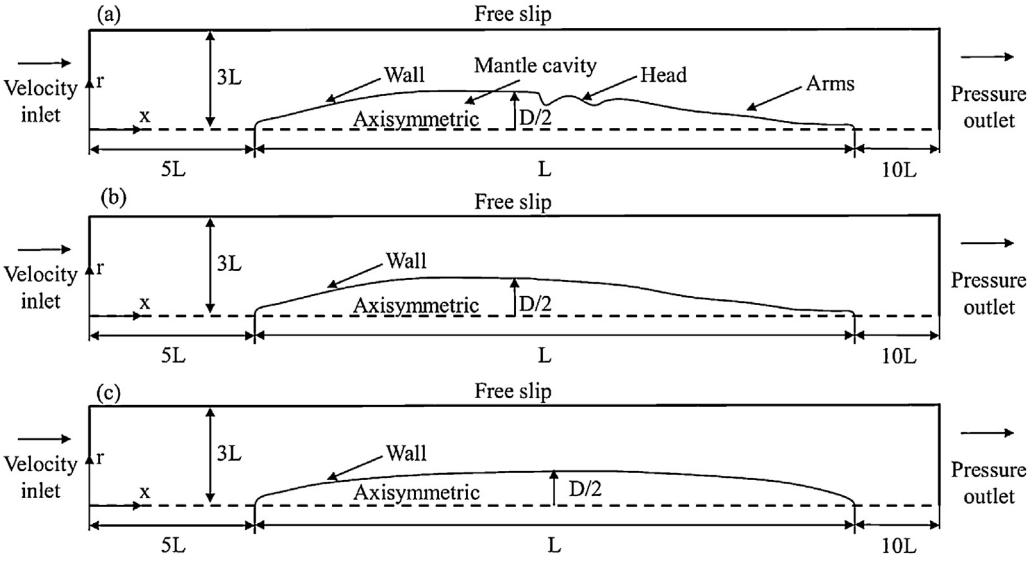

Fig. 6. Computational domain of a two-dimensional axisymmetric real squid (a), modified squid (b) and ellipse shaped (c) models and corresponding boundary conditions.

2.2. Computational model geometry, boundary conditions and meshing

A two-dimensional axisymmetric model was generated with the help of computed tomography scans of a real squid. When the real squid geometry was investigated, it was realized that a squid has two cavities located around her head as shown in Fig. 6(a). One of the cavities was between the squid's mantle cavity and head while the other was positioned between her head and arms. Although a squid has a well-known streamlined body shape, these two cavities probably have some influence on the flow characteristics around the squid. Therefore, additional two squid like geometries were generated by maintaining the squid's length and maximum body diameter the same. In this study, the body length (L) and diameter (D) of a two-dimensional axisymmetric squid, modified squid and ellipse-shaped squid models were 31 and 4.1 cm, respectively. Briefly, the modified squid shape model did not have any cavities around her head as shown in Fig. 6(b) and the remaining part of the geometry is identical with the real squid model. On the other hand, the ellipse shaped model given in Fig. 6(c) was formed with major and minor axes being equal to body length (L) and diameter (D), respectively.

An important parameter for streamlined bodies named fineness ratio were defined as the ratio of body length (L) to maximum body diameter (D) for the models and fineness ratio of three different bodies were determined to be $L/D = 7.56$. The length and height of computational domain were identified as 16L and 3L, respectively after domain independence simulations. Computational domain and boundary conditions are shown for the two-dimensional squid model in Fig. 6(a). The velocity inlet boundary condition was located at 5L upstream of the squid while pressure outlet boundary condition with zero gauge pressure was positioned at 10L downstream of the squid. Free-slip boundary condition was defined for upper side of the domain and the axis boundary condition was given for lower side of the solution domain to ensure axisymmetric simulation. Lastly, the squid's entire surface was defined as a wall with no-slip condition. All three numerical models were investigated by using commercial computational fluid dynamics (CFD) code ANSYS FLUENT 12.1 to identify the flow characteristics in solution domain. Specifically, pressure-based coupled algorithm was employed with SIMPLE scheme to the numerical model. Furthermore, second order upwind schemes were utilized for the advective terms of the transport equations. Criteria of convergence were set to 10^{-6} for the governing equations.

The velocity inlet boundary condition for acceleration of bodies was defined with two different UDF (user defined function) programs in the axial direction. Half period of the sine function was defined as a velocity profile for the inlet boundary condition to ensure that only positive velocity values were provided. Two different simulation times with $t = 0.5$ s and $t = 1$ s were determined to investigate the characteristics of fluid flow with time-dependent velocity passing through the fixed squid body. Sine velocity profiles shown in Fig. 7 were utilized for both $t = 0.5$ s and $t = 1$ s cases because earlier study [16] reported that mantle cavity pressure of a squid during fast swimming mode using electromyographic recordings exhibit pressure variation in the mantle cavity as a sine curve.

Flow characteristics around the squid models could be identified with an important non-dimensional number, named Reynolds number. In this work, the Reynolds number for all studied models was defined as $Re = \rho UL/\mu$. While the fluid's density and dynamic viscosity were ρ and μ, respectively, free stream velocity and the characteristic length (i.e., body length of squid models) were U and L, respectively. In here, length of all squid models were taken as 31 cm long and the highest velocity for a squid was chosen as 10 m/s to be consistent with the real conditions [16,17]. Since the flow with time-dependent velocity passing through the fixed squid body was investigated, Reynolds number for the studied cases varied from 0 to 3,090,727.

Tetrahedron and quadrilateral elements with high density mesh near the squid's body were placed in the solution domain of a real squid, modified squid and ellipse-shaped squid models to resolve high velocity gradient in the boundary layer. Final mesh was determined after different mesh partitions were considered. Furthermore, a mesh convergence test was performed for both drag force and total force in steady and unsteady solutions. Besides, time step size was chosen as 0.001 s after three different time step sizes of 0.01, 0.001 and 0.0001 s were considered. Total of 0.24–0.6 million elements were employed for all squid models. While Fig. 8(a) showed the elements on the solution domain, enlarged view of upstream near the squid model was given in Fig. 8(b). First cell from squid mantle wall was calculated and value of a non-dimensional wall-distance parameter y^+ was set to less than one for nodes nearest the wall. The first layer thickness was

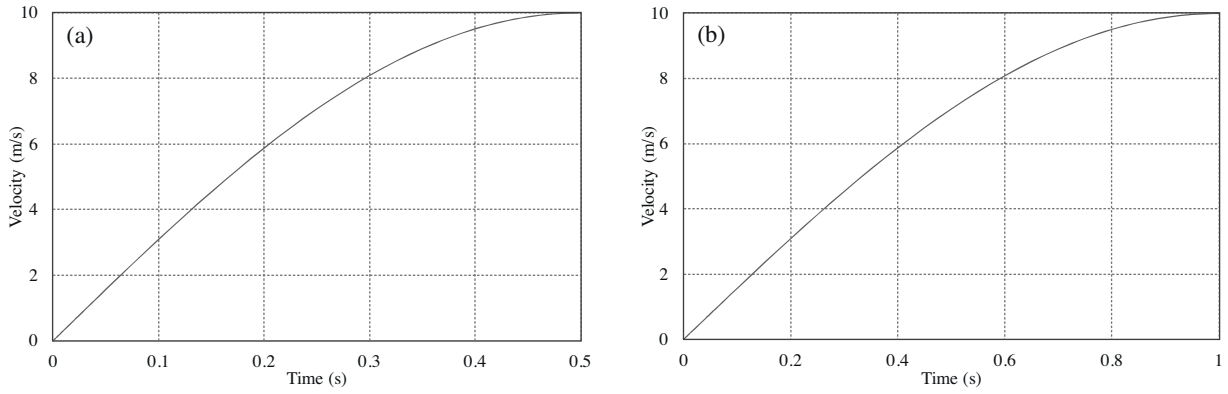

Fig. 7. Sine velocity program for $t = 0.5$ s (a) and $t = 1$ s (b) at inlet.

typically defined as $y^+ = (yu_\tau/\upsilon)$, where y could be expressed as $y = L \times y^+ \times \sqrt{80} \times Re_L^{-13/14}$.

2.3. Governing equations

Mixture of the k–ω model and the k–ε model were defined as shear stress transport (SST) k–ω model and Menter [18] reported that use of SST k–ω model is appropriate for high-Reynolds number flows with flow separation. Besides, the SST k–ω model is a two zone blending function model that standard k–ω model can be employed near the wall while k–ε model can be utilized in the outer part (far from the wall) of the boundary layer. In this study, investigation of a two-dimensional axisymmetric squid was performed during underwater swimming with the Reynolds-averaged Navier–Stokes (RANS) equations and SST k–ω models because it was a suitable choice for the high-Reynolds-number with flow separation. The value of y^+ was monitored and remained under unity since it was the most favorable y^+ value for the employed SST k–ω turbulence model for all numerical calculations. The unsteady Reynolds-averaged Navier–Stokes (RANS) is defined as

$$\frac{\partial \rho}{\partial t} + \frac{\partial}{\partial x_i}(\rho \bar{u}_i) = 0 \tag{1}$$

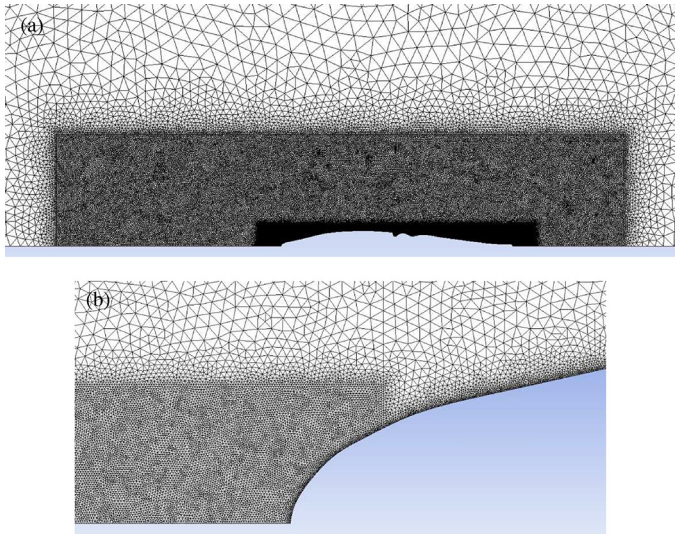

Fig. 8. Computational mesh of solution domain (a), enlarged view around squid surface (b).

$$\frac{\partial(\rho \bar{u}_i)}{\partial t} + \frac{\partial(\rho \bar{u}_i \bar{u}_j)}{\partial x_j} = -\frac{\partial \bar{p}}{\partial x_i} + \frac{\partial}{\partial x_j}\left[\mu\left(\frac{\partial \bar{u}_i}{\partial x_j} + \frac{\partial \bar{u}_j}{\partial x_i} - \frac{2}{3}\delta_{ij}\frac{\partial \bar{u}_l}{\partial x_l}\right)\right] + \frac{\partial}{\partial x_j}(-\rho\overline{u_i' u_j'}) \tag{2}$$

where $-\rho\overline{u_i' u_j'}$ is Reynolds stresses. The shear-stress transport (SST) k–ω Model is defined as

$$\frac{\partial}{\partial t}(\rho k) + \frac{\partial}{\partial x_i}(\rho k u_i) = \frac{\partial}{\partial x_j}\left(\Gamma_k \frac{\partial k}{\partial x_j}\right) + G_k + Y_k + S_k \tag{3}$$

$$\frac{\partial}{\partial t}(\rho \omega) + \frac{\partial}{\partial x_i}(\rho \omega u_i) = \frac{\partial}{\partial x_j}\left(\Gamma_\omega \frac{\partial \omega}{\partial x_j}\right) + G_\omega + Y_\omega + D_\omega + S_\omega \tag{4}$$

$$\Gamma_k = \mu + \frac{\mu_t}{\sigma_k} \quad \text{and} \quad \Gamma_\omega = \mu + \frac{\mu_t}{\sigma_\omega} \tag{5}$$

where G_k represents the generation of turbulence kinetic energy, G_ω represents the generation of ω, Γ_k, and Γ_ω represents the effective diffusivity of k and ω, respectively. Y_k and Y_ω represent the dissipation of k and ω, respectively due to turbulence and D_ω represents the cross-diffusion term while S_k and S_ω are user-defined source terms. Besides, μ_t is turbulent eddy viscosity while σ_k and σ_ω are constants [18].

2.4. Experimental validation

The real squid model obtained from CT images was built using 3D printer (ZORTRAX M200, Zortrax S.A., Poland). Then, this printed real squid model was used for PIV measurements. PIV experiments were performed in a large-scale open water channel with a length of 8000 mm and a width of 1000 mm. The test section of water channel was made from 15 mm thick transparent plexiglas sheet and the water was pumped into a settling chamber and passed through a honeycomb section and a two-to-one channel contraction before reaching the test chamber. Fig. 9 shows the 3D print out of real squid model placed into the test section. Black paint was sprayed on surface of the model to eliminate any reflection from the PIV lasers. Free stream turbulence intensity of the flow was less than 1.5% in the range of the studied Reynolds numbers. The laser sheet and squid model were located at 225 mm above the bottom surface of the channel while the water height was 450 mm during the tests. Nd:YAG lasers were used to generate a laser sheet that was perpendicular to the axis for the real squid model and the squid model's symmetry axis. A CCD camera having a resolution of 1600×1186 pixels was used to record the images. The seeding particles with a diameter of 10 μm in the flow were silver metallic coated hollow plastic spheres. The illuminating laser sheet thickness in the flow

Fig. 9. The side view of the squid in swimming position.

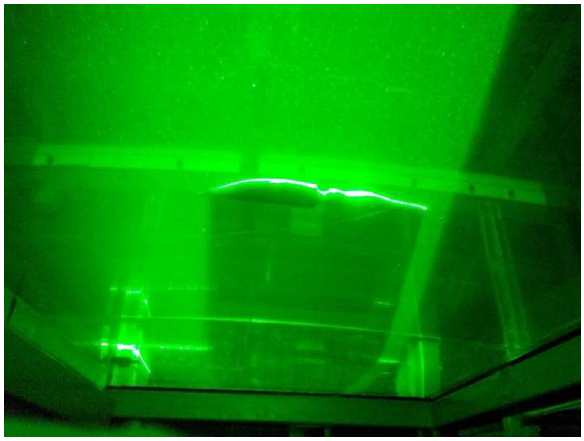

Fig. 10. The view of squid during PIV measurements.

field was approximately 1.5 mm as shown in Fig. 10. Dantec flow grabber digital PIV software employing the cross-correlation algorithm was used to compute the raw displacement vector field from the particle image data.

Contours of velocity field obtained from PIV and CFD were given in Fig. 11 for two different inlet velocities. The inlet velocities utilized in the experiments were used in CFD model so that comparison of PIV and CFD could be made. Due to the limitation of the open water channel, relatively lower velocities were tested; however, these inlet velocity boundary conditions were used in CFD model for the purpose of experimental validation. The velocity values around the mantle cavity of the printed real squid were compared for both PIV and CFD. The velocities around the mantle cavity were about 72–84 mm/s for inlet velocity of 78.6 mm/s (Fig. 11(a) and (b)) while the velocities around the mantle cavity were about 105–123 mm/s for inlet velocity of 115.7 mm/s (Fig. 11(c) and (d)). Therefore, the difference between PIV measurements and CFD.

3. Results and discussion

When a body in a fluid suddenly accelerates from rest, the body must overcome forces due to added mass and viscous effects inside the boundary layer in addition to the drag force. Briefly, the fluid in front of the body must be moved out of the way during acceleration of the body. The force required to move this fluid is directly related to shape of the body and called added mass force. Besides, another force named basset force appears on the development of the body's boundary layer when the body is exposed to a rapid acceleration. Therefore, a body is required to produce a thrust larger than total of these forces ($F_{Total} = F_{Drag} + F_{Added\,mass} + F_{Basset}$) so that it can follow the desired or commanded velocity programs. Particularly, when flow around a squid is considered, calculation of these forces plays a key role in determination of required thrust.

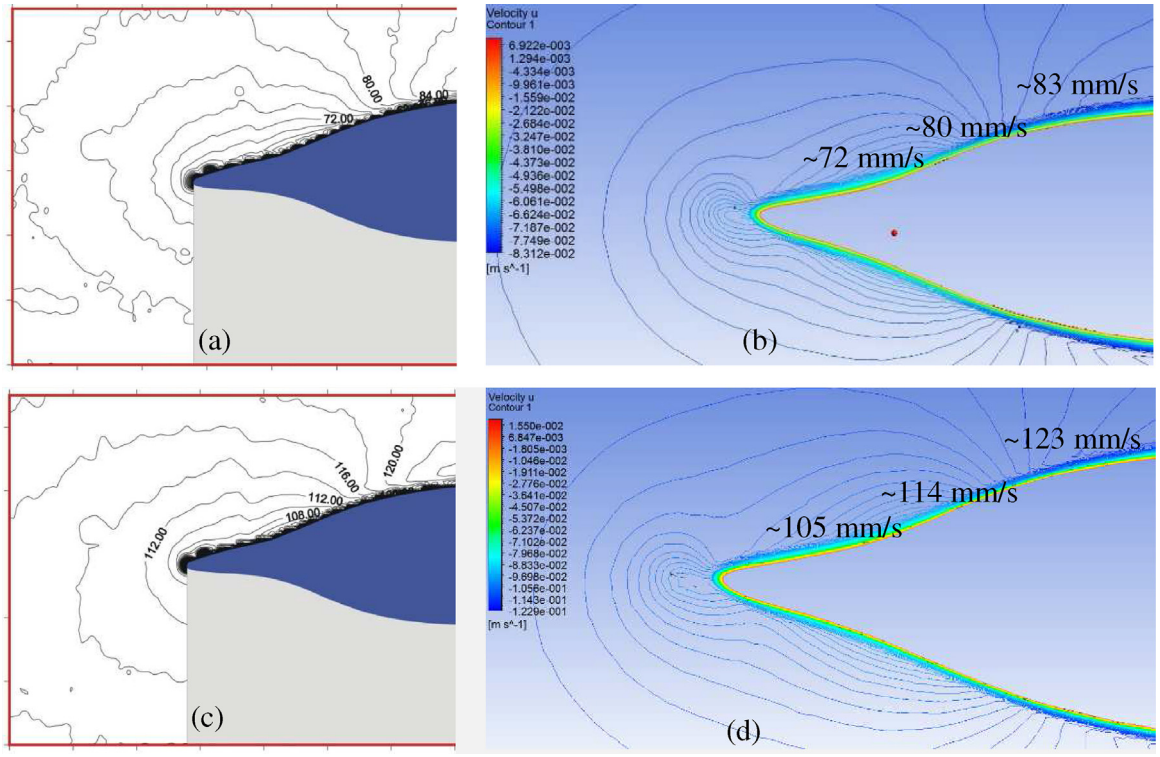

Fig. 11. Comparison of PIV (a, c) and CFD (b, d) velocity contour plots for inlet velocities of 78.6 and 115.7 mm/s.

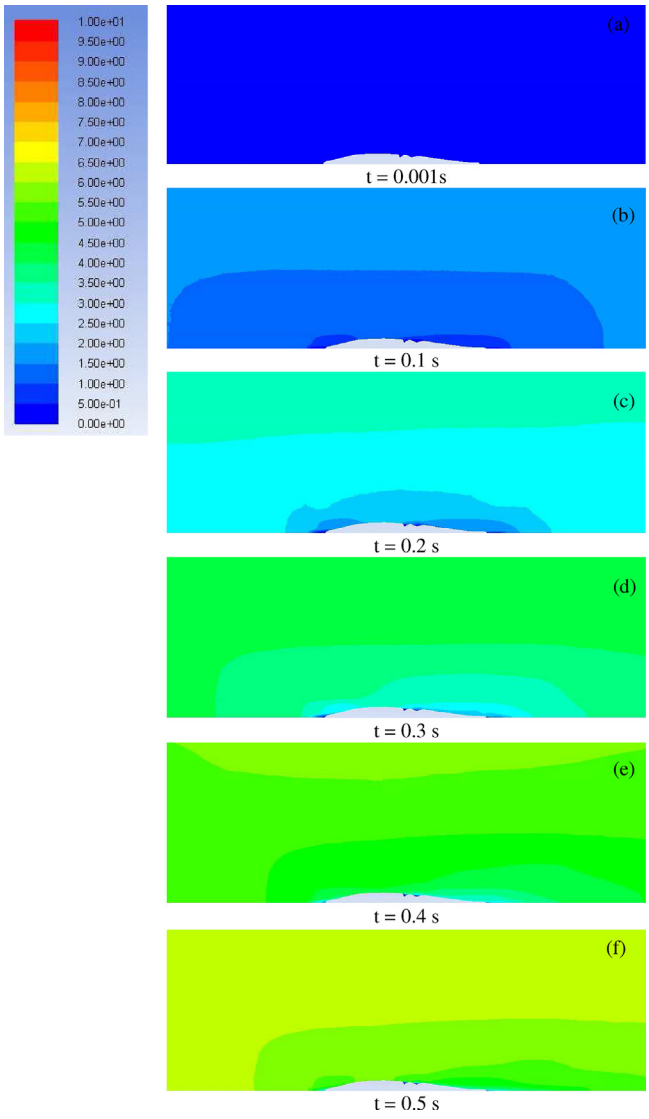

Fig. 12. Velocity contour plots around the real squid model during Sine velocity program (t = 0.5 s). t = 0.001 s (a), t = 0.1 s (b), t = 0.2 s (c), t = 0.3 s (d), t = 0.4 s (e), t = 0.5 s (f). Legend shows the values of velocity in the range of 0 and 10 m/s.

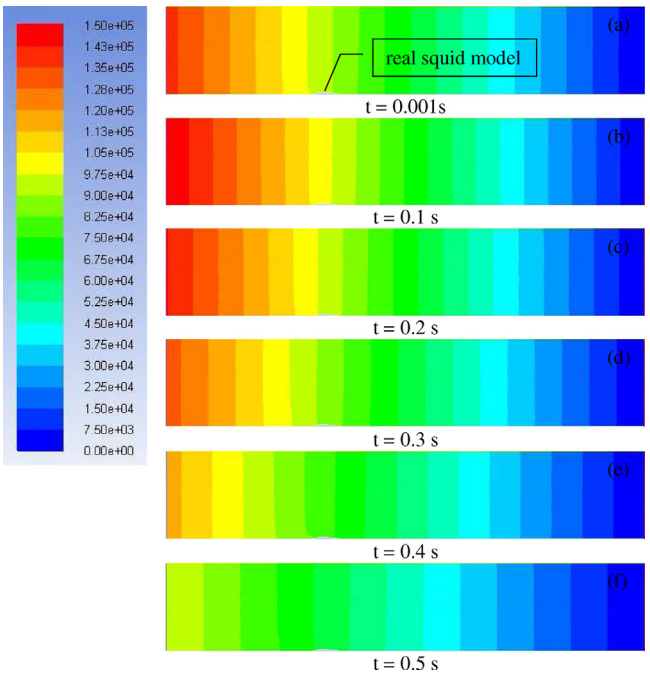

Fig. 13. Pressure contour plots of solution domain during Sine velocity program (t = 0.5 s). t = 0.001 s (a), t = 0.1 s (b), t = 0.2 s (c), t = 0.3 s (d), t = 0.4 s (e), t = 0.5 s (f). Legend shows the values of pressure in the range of 0 and 150,000 Pa.

3.1. Mean velocity and pressure variation around the squid model

In this study, the squid was fixed while time dependent inlet velocity was defined to simulate the squid's swimming performance. The time averaged velocity contours around the squid were plotted in Fig. 12 to eliminate the transient characteristics of the flow, which may not accurately represent the studied time period. It was realized that velocity contour values in front of the squid increased until the end of velocity program indicating that the fluid (namely, added mass) in front of the squid was also accelerated. The fluid at the back of the squid was also raised to be able to satisfy continuity equation.

Similarly, the time averaged pressure contours at the solution domain were plotted in Fig. 13. When the flow around a squid was investigated, there is a large pressure gradient in the calculation domain (Fig. 13) especially in earlier simulation times. The reason for having large pressure gradient can be explained from total pressure point of view because total pressure has both static and dynamic pressure components. Firstly, static pressure appears large in Fig. 13 at t = 0.001, 0.1 and 0.2 since the dynamic pressure component in the total pressure was not significant due to the fact that inlet velocity was small at those times. Secondly, once the inlet velocity increases, dynamic pressure also rises in the amount of $0.5 * \rho * V^2$ and provides significant contribution to the total pressure. Therefore, the decrease in static pressure can be observed at t = 0.3, 0.4 and 0.5 s.

The localized pressure distribution around the squid was plotted in Fig. 14. It was noted that the mean pressure difference between front and back of the squid was highest at the beginning of the motion implying larger pressure drag. When velocity program reached 0.5 s, the mean pressure difference across the squid decreased and almost became insignificant indicating that pressure drag only played a key role during early acceleration phase of the squid.

In addition to mean velocity and pressure contours, instantaneous velocity and vorticity contours were plotted in Fig. 15 for two different times, namely t = 0.1 s and t = 0.5 s. It was revealed that circulating regions were formed near the head region as observed from both velocity and vorticity contour plots. Besides, the velocity above the squid reached about 10 m/s (Fig. 15(b)) when velocity program ended.

3.2. Forces acting on squid models

In this study, drag, added mass and basset forces on a real squid, a modified squid and an ellipse-shaped models were numerically investigated for two different commanded velocity programs. Drag force consists of pressure and viscous drags [19,20] and it was given by

$$F_D = F_{D\_pressure} + F_{D\_viscous} \tag{6}$$

Here, drag due to pressure was calculated from $F_{D\_pressure} = 2\pi \int_0^l p * (r * \sin\alpha) dx$ while drag due to viscous was obtained from $F_{D\_viscous} = 2\pi \int_0^l p * (r * \cos\alpha) dx$. Here, p and τ are the pressure normal to the body's surface and the shear stress tangent to the body's surface, respectively. While r is the radius from the axis of the body surface, α is the arc length along the meridian profile and L_m is

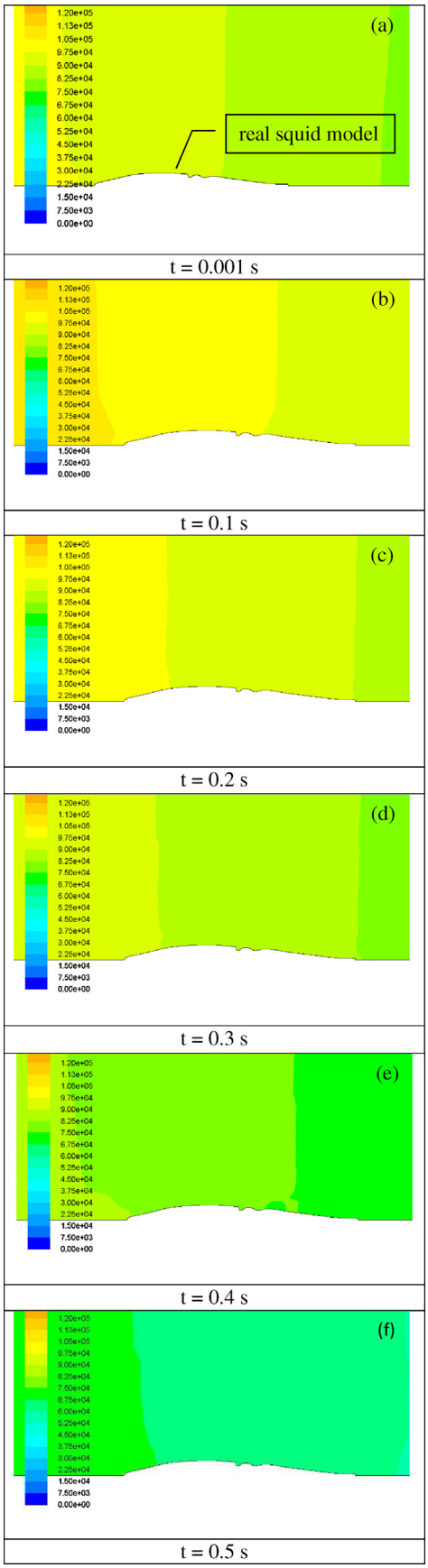

Fig. 14. Localized pressure contour plots of fluid flow around the squid during Sine velocity program ($t = 0.5$ s). $t = 0.001$ s (a), $t = 0.1$ s (b), $t = 0.2$ s (c), $t = 0.3$ s (d), $t = 0.4$ s (e), $t = 0.5$ s (f). Legend shows the values of pressure in the range of 0 and 150,000 Pa.

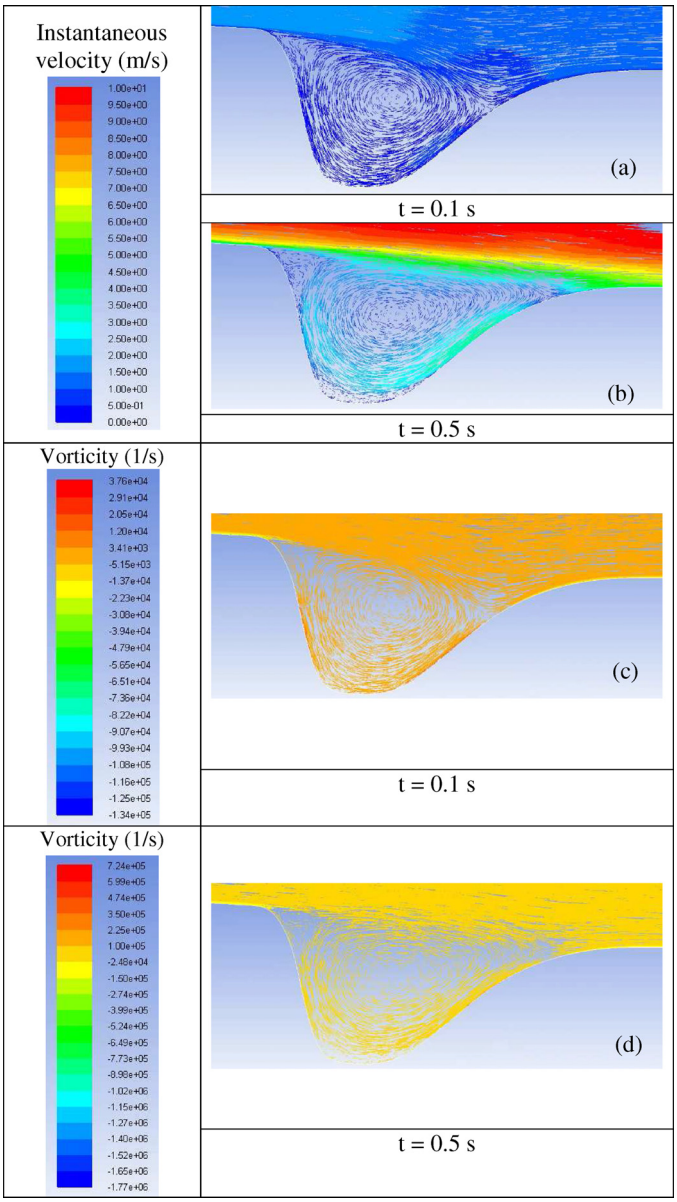

Fig. 15. Instantaneous velocity (m/s) contour at $t = 0.1$ s (a), at 0.5 s (b); vorticity (1/s) contour at $t = 0.1$ s (c), at 0.5 s (d).

the total arc length of the body models. Total drag force due to pressure and viscous drag forces were numerically analyzed for squid models during acceleration phase and drag coefficients were obtained.

Added mass force calculations were performed for all three models. Firstly, the added mass coefficient (a_{11}) was obtained from the added mass coefficient diagram provided by Korotkin [5] based on the length and diameter of the models with the assumption of an ellipsoidal shape. Then, the volume of each model (V_m) was attained with the help of design modeler module of Ansys 12.1 [21]. Lastly, added mass force was calculated using $F_A = a_{11}\rho V_m(du/dt)$. Here, $a_{11}\rho V_m$ is added mass while du/dt is acceleration of the body. When a squid accelerates impulsively, development of a boundary layer on the squid surface is lagged and velocity gradient inside the boundary layer varies rapidly resulting in the basset force to arise. In the current study, basset forces on the squid models were calculated based on an acceleration of a flat plate [22]. Basset force calculations for the models provide a reasonable estimation since

squid models have streamlined shapes. Basset force due to boundary layer development was given by

$$F_B = A_{surface}\sqrt{\frac{\rho_c \mu_c}{\pi}}\int_0^t \frac{du/dt'}{\sqrt{t-t'}}dt' \tag{7}$$

where, $A_{surface}$ is surface area of the squid, ρ_c is the carrier fluid's (i.e., water's) density, μ_c is viscosity of the fluid, $u(t)$ is velocity of the body, t is total acceleration time and t' is being the instantaneous time.

3.3. Determination of coefficients and forces

Variation of total force coefficient, also named a thrust force coefficient, and drag force coefficient are shown in Tables 1 and 2 during acceleration of squid models for two different velocity programs. Increase in the Reynolds number is given in the second column of both tables since all models accelerate as the time passes. The CFD solver provided thrust force that had drag, added mass, basset and inertial forces. Added mass and basset forces were calculated to determine the effect of these forces on an accelerating squid. The weigh of both added mass and basset forces remained less than 4% for all three models and this indicated that these forces arising for unsteady flows could be insignificant when the bodies have streamlined shape as in squid model cases. It was noted that total and drag force coefficients were highest in the ellipse-shaped model during initiation of movement while the real squid model had the lowest value for the same duration. This can be explained by pressure force which was highest in ellipse-shaped model compared to other models because the tip of a real squid had more streamlined profile than ellipse-shaped model. Total and drag force coefficients became highest for the real squid model while the other two models exhibited lower coefficient values for later times in the velocity program. This can be due to the fact that the real squid body had small cavities around her eyes and these cavities may cause flow separation and this may lead to higher total and drag force coefficients.

In addition to experimental validation discussed in previous section Malazi et al. [23] performed a numerical study on a longfin inshore squid's swimming characteristics to determine drag coefficient for different species of underwater swimmers at different *Re* numbers. They reported that drag coefficients for squid model with $L/D = 7.56$ were 0.003996, 0.003712 and 0.003244 for the Reynolds numbers of 1.0E6, 1.6E6 and 2.9E6, respectively. These drag coefficients [23] agree well with the drag coefficients obtained in the present study.

Total force needed to follow commanded velocity programs on squid models were calculated and plotted in Figs. 16 and 17. It was realized that all squid models were required to provide large amount of forces to overcome added mass, basset and drag forces initially. Once the squid models reaches about half of their velocity program duration, total force required to track the desired velocity program starts to decrease. The reason behind this decline may be due to the fact that pressure variation along the squid models changes and the effect of pressure drag may be lower when the acceleration of squid models decreases. Besides, added mass initially present in front of the squid models has already been pushed out of the way so that contribution of added mass force to the total force becomes negligible. It was also noted that ellipse shaped squid model exhibits larger force requirements to follow the velocity programs up to 0.4 and 0.6 s in Figs. 16 and 17, respectively compared to the other two models. This is probably because of the pressure drag as pressure variation along the ellipse shape is different than the other models. Especially, the existence of mantle cavity gives squid models a priceless advantage of a streamlined body while the ellipse shape seems to behave a like blunt body at the first half of the

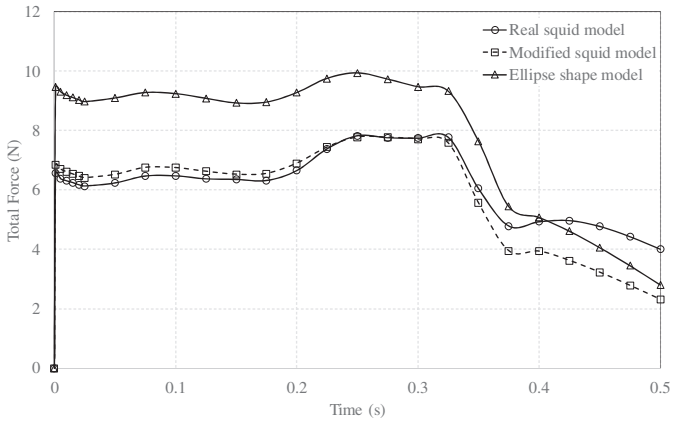

Fig. 16. Variation of total force during acceleration of squid models between 0 and 0.5 s.

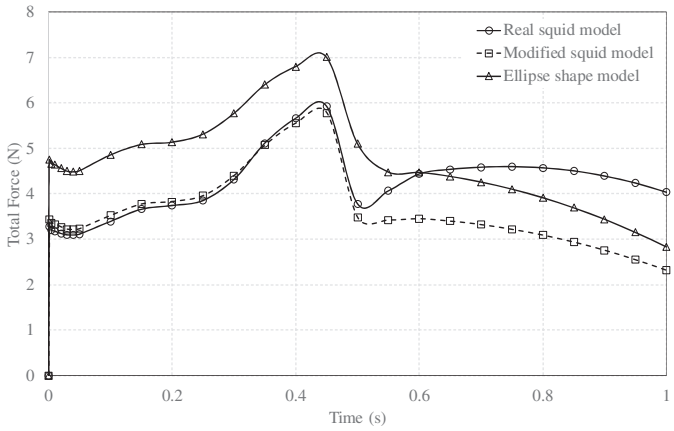

Fig. 17. Variation of total force during acceleration of squid models between 0 and 1.0 s.

movement. On the other hand, the real squid model shows a larger force requirement than the other two models at the last quarter of velocity program. This may be due to the flow separation taking place around the squid's head in the real squid model while ellipse shaped and modified squid models do not have cavities around the head area. When total force variations are considered, modified squid models without cavities around the head provide promising results (i.e., lower force requirement) to be used for the design of an underwater vehicle.

3.4. Determination of jet velocities based on different nozzle diameters

When a body needs to move in a fluid, the body must generate certain amount of thrust to follow a desired velocity program. Especially, if this body starts to move from rest and needs to track the desired velocity program with changing acceleration, it would need to produce thrust overcoming added mass and basset forces as well as drag forces. The thrust force calculation for squid models were discussed in the previous section. However, control volume (CV) analysis was performed to calculate the jet velocity accurately by taking the entire solution domain (Fig. 18) as a control volume:

$$\frac{\partial}{\partial t}\int_{CV}\rho u dV + \int_{CS}\rho u(u-s)\cdot\vec{n}dS = \sum F_{CV} \tag{8}$$

The first integral on left hand side of Eq. (8) is related to the time rate of change of u within the control volume due to unsteadiness while the second integral on left hand side of Eq. (8) is associated

Table 1
Total and drag force coefficients for real squid, modified-squid and ellipse-shaped squid models when t is between 0 and 0.5 s.

Time (s)	Reynolds number (Re)	Drag force coefficient of a real squid	Drag force coefficient of a modified squid	Drag force coefficient of an ellipse shaped squid	Total force coefficient of a real squid	Total force coefficient of a modified squid	Total force coefficient of an ellipse shaped squid
0	0	0	0	0	0	0	0
0.1	954,619	0.052848	0.054344	0.060318	0.053768	0.055284	0.061355
0.2	1,815,888	0.015047	0.015399	0.016774	0.015269	0.015626	0.017023
0.3	2,499,583	0.009294	0.009131	0.009075	0.009382	0.009221	0.009174
0.4	2,938,848	0.004281	0.003368	0.003512	0.004318	0.003406	0.003553
0.5	3,090,727	0.003168	0.001804	0.001769	0.003171	0.001807	0.001774

Table 2
Total and drag force coefficients for real squid, modified-squid and ellipse-shaped squid models when t is between 0 and 1.0 s.

Time (s)	Reynolds number (Re)	Drag force coefficient of a real squid	Drag force coefficient of a modified squid	Drag force coefficient of an ellipse shaped squid	Total force coefficient of a real squid	Total force coefficient of a modified squid	Total force coefficient of an ellipse shaped squid
0	0	0	0	0	0	0	0
0.2	954,619	0.030573	0.030849	0.033534	0.031062	0.031348	0.034075
0.4	1,815,888	0.012875	0.012463	0.012343	0.012994	0.012584	0.012475
0.6	2,499,583	0.005324	0.00407	0.004272	0.005372	0.004119	0.004325
0.8	2,938,848	0.003983	0.002647	0.002716	0.004004	0.002668	0.002739
1	3,090,727	0.003192	0.001806	0.001789	0.003194	0.001808	0.001792

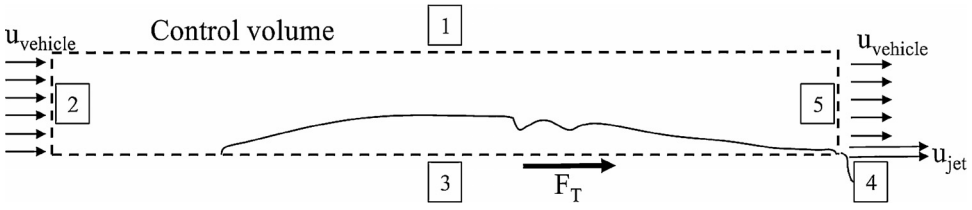

Fig. 18. Control volume of the squid model.

with the net flux of u out of the control surface. In here, u is not a function of control volume; so it can be taken out of the integral and ρ is constant. Besides, integral over the entire control surface can be expanded as given in Eq. (9):

$$\frac{\partial u}{\partial t}\int_{CV}\rho dV + \int_1 \rho u(u-s)\cdot\vec{n}dS + \int_2 \rho u(u-s)\cdot\vec{n}dS + \int_3 \rho u(u-s)\cdot\vec{n}dS + \int_4 \rho u(u-s)\cdot\vec{n}dS + \int_5 \rho u(u-s)\cdot\vec{n}dS = \sum F_{CV} \tag{9}$$

In here, $(u-s)$ was velocity of the system boundary relative to control surface and $(u-s)\cdot\vec{n}$ was normal component of the relative velocity; therefore, surface integrals 1 and 3 became zero because velocity of system boundary and relative velocity were perpendicular to each other. Besides, surface integrals 2 and 5 were zero since velocity of system boundary and control surface were equal at these surfaces. As a result,

$$m_{CV}\frac{\partial u}{\partial t} + \int_4 \rho u_{jet}(u_{jet}-u_{vehicle})\cdot\vec{n}dS = \sum F_{CV} \tag{10}$$

When ρ and dS were taken out from surface integral 5 and the equation was reorganized, Eq. (11) could be obtained as

$$\rho A_{jet}u_{jet}(u_{jet}-u_{vehicle}) = F_D + F_B + F_A - m_{CV}\frac{\partial u}{\partial t} \tag{11}$$

The right hand side of Eq. (11) was lumped as total force (i.e., drag, basset, added and inertial forces) acting on control volume and this force was calculated by CFD solver. Therefore, $F_T = \rho A_{jet}u_{jet}(u_{jet}-u_{vehicle})$, could be used to obtain required jet velocity once the total thrust force was known. Here, ρ was density of the fluid and 1000 kg/m^3 was used since the working fluid was water, A_{jet} was cross-sectional area of the jet and u_{jet} and $u_{vehicle}$ were the velocity of the jet and the vehicle, respectively. It was noted that the thrust force driving underwater vehicles directly depends on the jet velocities.

A squid is known to be from the family of cephalopods in the underwater world and typically uses her mantle cavity along with her nozzle for locomotion in water. Briefly, a squid pulls the water into her mantle cavity from the openings located near her head prior to move. Then, she contracts her mantle cavity wall by building up pressure inside to eject the water thru her nozzle backward and she gains large acceleration in the opposite (i.e., forward) direction. Although high pressure inside a mantle cavity of a squid has capability to compress the water, a nozzle of a squid plays a key role to obtain required thrust the squid needs. Particularly, a squid has a quite unique nozzle with a flexible tissue allowing fluid (i.e., water) to exit from the mantle cavity only in one direction (i.e., toward the outside). Furthermore, a squid can change her nozzle diameter during under water swimming. Therefore, in this part of the study we are interested in the effect of a nozzle diameter on a squid's jet velocity. Nozzle diameter of the squid used in the simulations was measured to be 1 cm. It was realized that diameter of nozzle can expand or contract due to its muscular tissue structure. Therefore, 2 cm (0.02 m), 1 cm (0.01 m) and 0.5 cm (0.005 m) nozzle diameters were chosen to investigate the relation among the jet velocity of the real squid, the modified and the ellipse shaped squid models. A_{jet} values were calculated to be 3.1417E−4, 7.8539E−05 and

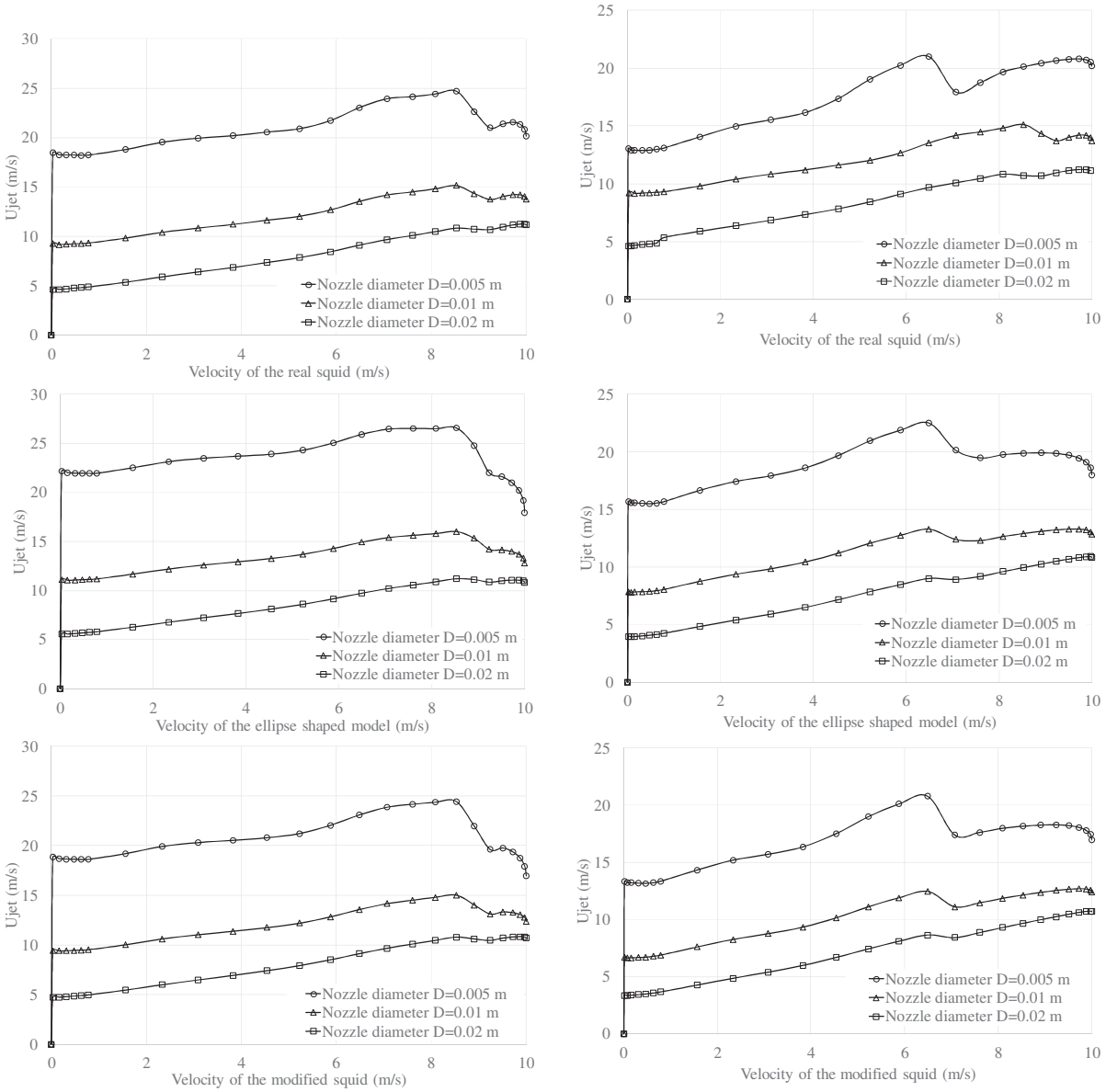

Fig. 19. Effect of three different diameters on jet velocity for two different velocity programs of the real squid (top (a and b)), ellipse shaped (middle (c and d)) and modified squid (bottom (e and f)) models (a, c and e results are for velocity program with $t = 0–0.5$ s while b, d, and f results are for velocity program with $t = 0–1.0$ s).

1.9635E−05 m^2 for the nozzle diameters of 0.02, 0.01 and 0.005 m, respectively. Therefore, Fig. 19 shows the effect of different nozzle diameters to the jet velocity for squid swimming velocities up to 10 m/s. It is noted that when diameter of a nozzle becomes 0.005 m during water ejection, all of the squid models would require largest jet velocities to sustain the same squid speed. This implies that an underwater vehicle resembling a squid shape should have a nozzle diameter around 0.02 m because larger nozzle diameter seems to cause smaller jet velocities. This probably leads to a more efficient underwater vehicle.

3.5. Jet efficiency study

When an underwater transportation is considered, the jet efficiency is an important parameter to evaluate performance of an underwater vehicle. Moslemi and Krueger [9] explained jet efficiency parameter using propulsive efficiency that could be quantified as $\eta = \frac{2}{1+(U_{jet}/U_{vehicle})}$. Here, $U_{vehicle}$ is the underwater vehicle's velocity while U_{jet} stands for the jet velocity of the vehicle. Fig. 20 shows propulsive efficiency results of the real, ellipse shaped and modified squid models for nozzle diameters of 0.005, 0.01 and 0.02 m at two different velocity programs. It is documented that the propulsive efficiency is the highest when the nozzle diameter is 0.02 m for all models regardless of the followed velocity programs. Besides, propulsive efficiency at nozzle diameter of 0.02 m is two to three times larger in magnitude than propulsive efficiency at nozzle diameter of 0.005 m for all bodies. This implies that the use of a larger size nozzle strongly contributes to higher propulsive efficiency. The results also demonstrated that the propulsive efficiency of the modified squid model is slightly more than the propulsive efficiency of other models because the modified squid model has a more streamlined body shape than both the real squid and ellipse shape models. It was also noted that the propulsive efficiency of the modified squid can be nearly 10% and 4% more effective than the ellipse shaped and real squid models, respectively.

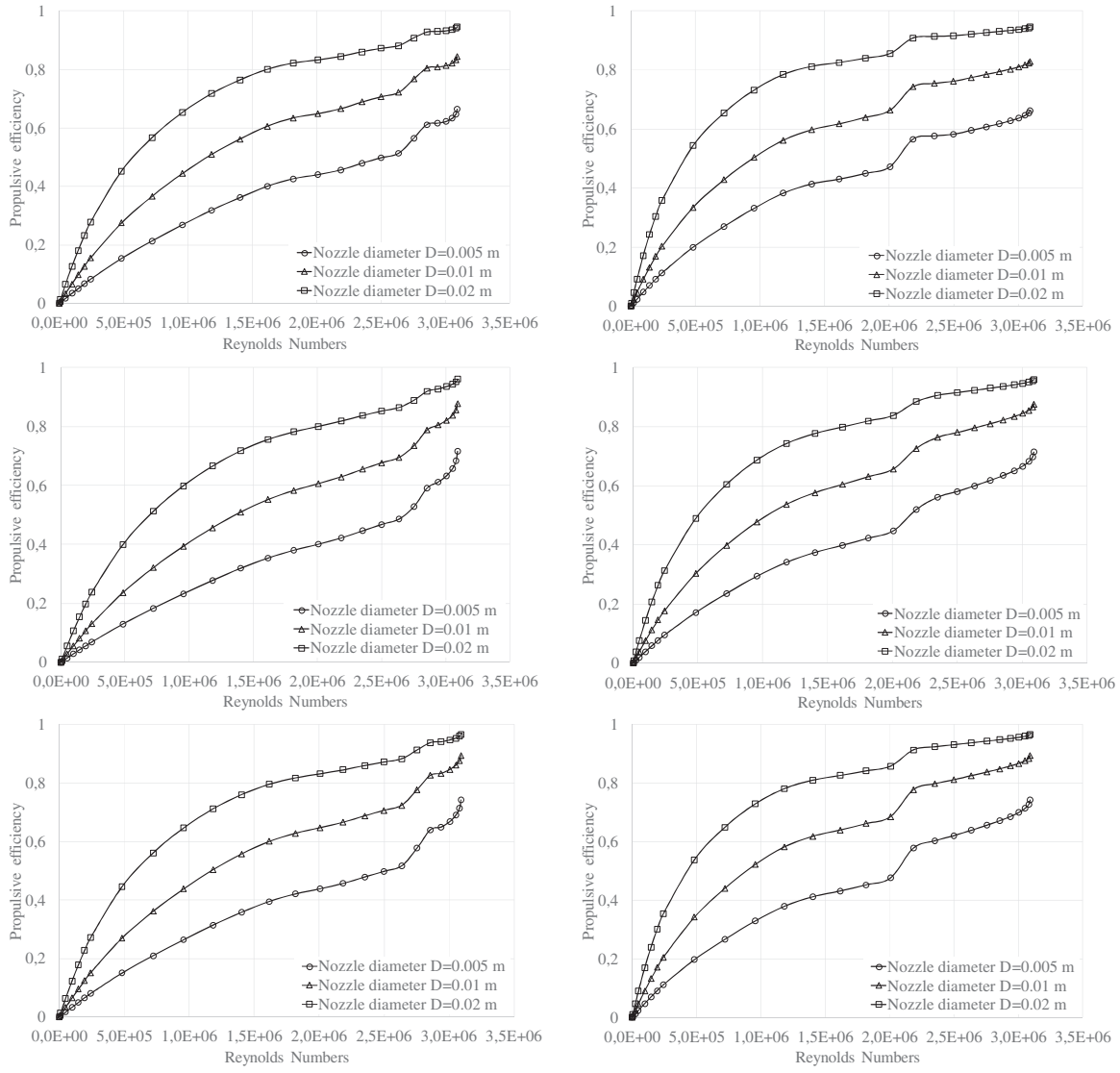

Fig. 20. Propulsive efficiency variation with Reynolds number of three different diameters for two different velocity programs of the real squid (top (a and b)), ellipse shaped (middle (c and d) and modified squid (bottom (e and f) models (left column results are for velocity program with $t = 0–0.5$ s while right column results are for velocity program with $t = 0–1.0$ s).

4. Conclusion

This study investigates swimming characteristics of squid like models numerically. Particularly, a real squid, ellipse shaped and modified squid models were set to motion from rest by following a desired velocity program. It was realized that although models look similar to each other, the forces they were exposed to during acceleration were quite different. The total force combination of drag force, added mass and basset forces were introduced and calculated for two different velocity programs. It was noted that all models suffered from pressure drag during the early stage of their motion and the modified squid model required less thrust force than other two models to reach the same commanded velocity program. The effect of the nozzle diameter was also examined in this study and it was documented that a larger nozzle diameter provided higher propulsive efficiency values. It was concluded that hydrodynamic characteristics of the studied bodies can explain the behavior of a body at various velocities under the water and provide valuable design parameter information on an underwater vehicle.

Acknowledgements

This work has been supported by TUBITAK (The Scientific and Technological Research Council of Turkey) under 3501 Program, Project #: 111M598. Authors would also like to thank Dr. Gökhan Gökçen for his support in obtaining CAD model of the squid from computed tomography images.

References

[1] Bartol IK, Gharib M, Weihs D, Webb PW, Hove JR, Gordon MS. Body-induced vortical flows: a common mechanism for self-corrective trimming control in boxfishes. J Exp Biol 2005;208:327–44.
[2] Stelle LL, Blake RW, Trites AW. Hydrodynamic drag in steller sea lions (*Eumetopias Jubatus*). J Exp Biol 2000;203:1915–23.
[3] Lin Z, Liao S. Calculation of added mass coefficients of 3D complicated underwater bodies by FMBEM. Commun Nonlinear Sci Numer Simulat 2011;16:187–94.
[4] Ghassemi H, Yari E. The added mass coefficient computation of sphere, ellipsoid and marine propellers using boundary element method. Pol Maritime Res 2011;18:17–26.
[5] Korotkin AI. Added mass of ship structure. Fluid mechanics and its applications. New York: Springer; 2009.

[6] Jagadeesh P, Murali K. RANS predictions of free surface effects on axisymmetric underwater body. Eng Appl Comput Fluid Mech 2010;4:301–13.
[7] Anderson EJ, Grosenbaugh MA. Jet flow in steadily swimming adult squid. J Exp Biol 2005;208:1125–46.
[8] Stewart WJ, Bartol LK, Krueger PS. Hydrodynamic fin function of briet squid, *Lolliguncula brevis*. J Exp Biol 2010;213:2009–24.
[9] Moslemi AA, Krueger PS. Propulsive efficiency of a biomorphic pulsed jet underwater vehicle. Bioinsp Biomim 2010;5:036003, 14 pp.
[10] Moslemi AA, Krueger PS. The effect of Reynolds number on the propulsive efficiency of a biomorphic pulsed jet underwater vehicle. Bioinsp Biomim 2011;6:026001, 11 pp.
[11] Shereena SG, Vengadesan S, Idichandy VG, Bhattacharyya SK. CFD study of drag reduction in axisymmetric underwater vehicles using air jets. Eng Appl Comput Fluid Mech 2013;7:193–209.
[12] Mansoorzadeh SH, Javanmard E. An investigation of free surface effects on drag and lift coefficients of an autonomous underwater vehicle (AUV) using computational and experimental fluid dynamics methods. J Fluids Struct 2014;51:161–71.
[13] Bettle MC, Gerber AG, Watt GD. Using reduced hydrodynamic models to accelerate the predictor–corrector convergence of implicit 6-DOF URANS submarine maneuvering simulations. Comput Fluids 2014;102:215–36.
[14] Nematollahia A, Dadvandb A, Dawoodian M. An axisymmetric underwater vehicle-free surface interaction: a numerical study. Ocean Eng 2015;96:205–14.
[15] Randeni P, Leonga ZQ, Ranmuthugalaa D, Forresta AL, Duffy J. Numerical investigation of the hydrodynamic interaction between two underwater bodies in relative motion. Appl Ocean Res 2015, http://dx.doi.org/10.1016/j.apor.2015.02.006.
[16] Gosline JM, DeMont ME. Jet-propelled swimming in squids. Sci Am 1985;256:96–103.
[17] Thompson JT, Bartol IK, Baksi AE, Li KY, Krueger PS. The ontogeny of muscle structure and locomotory function in the long-finned squid *Doryteuthis pealeii*. J Exp Biol 2010;213:1079–91.
[18] Menter FR. Two-equation Eddy-viscosity turbulence models for engineering applications. AIAA J 1994;32(8):1598–605.
[19] Karim M, Rahman M, Alim A. Numerical computation of viscous drag for axisymmetric underwater vehicles. Jurnal Mekanikal 2008;26:9–21.
[20] Vasudev KL, Sharma R, Bhattacharyya SK. A multi-objective optimization design framework integrated with CFD for the design of AUVs. Methods Oceanogr 2014;10:138–65.
[21] ANSYS Inc., Lebanon, USA. User's guide documents for ANSYS FLUENT 12.1.
[22] White FM. Viscous fluid flow. New York: McGraw Hill; 2006.
[23] Malazi MT, Okbaz A, Olcay AB. Numerical investigation of a longfin inshore squid's flow characteristics. Ocean Eng 2015;108:462–70.